Surface & Coatings Technology 476 (2024) 130191

Contents lists available at ScienceDirect

Surface & Coatings Technology

journal homepage: www.elsevier.com/locate/surfcoat

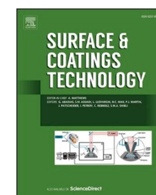

Reactively grown Al/Si-based top coatings protecting TM-diborides (TM = W, Ti, Hf) against high-temperature oxidation

S. Richter [a,*], T. Glechner [a], T. Wojcik [a], B. Widrig [b], S. Kolozsvári [c], P. Polcik [c], O. Hunold [b], L. Zauner [a], J. Ramm [b], H. Riedl [a,d]

[a] Christian Doppler Laboratory for Surface Engineering of high-performance Components, TU Wien, A-1060 Wien, Austria
[b] Oerlikon Balzers, Oerlikon Surface Solutions AG, FL-9496 Balzers, Liechtenstein
[c] Plansee Composite Materials GmbH, D-86983 Lechbruck am See, Germany
[d] Institute of Materials Science and Technology, TU Wien, A-1060 Wien, Austria

ARTICLE INFO

Keywords:
Diborides
PVD
Protective coatings
Oxidation
Silane

ABSTRACT

Architectural designs involving Al- and/or Si-containing top coatings present an effective approach to protect oxidation-sensitive materials such as binary transition metal (TM) diborides against high-temperature oxidation. Using reactive arc evaporation, Al-Si-N, Al-Si-O, and Si-O top coatings were applied on sputter-deposited $WB_{1.9}$, $TiB_{2.7}$, and $HfB_{2.4}$ thin films, respectively. A pure Si adhesion layer was introduced prior to the deposition of both oxide-based top coatings (Al-Si-O & Si-O) to prevent *in-situ* oxidation of the diboride base layers. During thermal annealing up to 1200 °C, Al-Si-O and Si-O provided outstanding oxidation resistance on top of $TiB_{2.7}$ and $HfB_{2.4}$, while limited adhesion was observed on $WB_{1.9}$ at elevated temperatures. Contrary, Al-Si-N protected architectures suffered from accelerated oxidation beyond 800 to 1000 °C. Isothermal annealing in ambient air at 1200 °C for 30 h confirmed the long-term stability of the oxide-based top coatings, revealing no decohesion or oxygen inward diffusion beyond the Si interlayer. Complementary TEM analysis showed that the Si-O top coating forms a dense SiO_2 scale above the columnar $HfB_{2.4}$, while the formation of a mullite scale ($3Al_2O_3{\cdot}2SiO_2$) and pronounced recrystallization is recorded for the Al-Si-O protected $HfB_{2.4}$. In summary, the Al-Si-O- and Si-O-based top coatings demonstrated exceptional high-temperature oxidation resistance, fully protecting the TM-diborides from oxidative attack.

1. Introduction

Decreasing the environmental footprint is of utmost importance when striving for more sustainable industrial processes and products. Besides the focus on decarbonization and reduced primary energy consumption, extending the lifetime of high-performance components is considered as a highly efficient approach [1]. In this context, physical vapor deposited protective coatings offer attractive possibilities to extend the operating range of highly stressed materials by enhancing the surface hardness, corrosion-, wear-, and in particular the high-temperature oxidation resistance [2].

Research on novel protective coatings withstanding extreme mechanical and thermal loads is strongly focused on the class of ultra-high temperature ceramics (UHTCs) such as transition metal diborides. In addition to their outstanding thermal stability with melting temperatures beyond 3000 °C, TM-diborides feature excellent wear and creep resistance, as well as super-hardness and chemical inertness [3–6]. Their suitability for applications under extreme thermal and mechanical loads [7,8] is proven by today's use in *e.g.*, atmospheric reentry vehicles, gas turbine combustors, or rocket engine nozzles [4–6,9].

Despite their outstanding mechanical properties, the application of TM-diborides as protective thin films is generally limited due to their poor oxidation resistance related to the competitive growth of volatile boron- and porous TM-oxides [10]. For unalloyed diboride based thin films, the adverse volatilization of B_2O_3 as well as the formation of porous TM-oxides is predominantly observed between 400 and 800 °C [11–13]. Interestingly, these environmental reactions are shifted to higher temperatures for bulk TM-diborides, which is mainly attributed to altered oxidation kinetics and microstructural differences (*i.e.*, boron-rich grain boundary phases) [14–17].

To improve the oxidation resistance of bulk TM-diborides, an approach *via* co-sintering of Si-based compounds (*e.g.*, *SiC*, $MoSi_2$, *etc.*) is

* Corresponding author.
E-mail address: sophie.richter@tuwien.ac.at (S. Richter).

https://doi.org/10.1016/j.surfcoat.2023.130191
Received 24 July 2023; Received in revised form 27 October 2023; Accepted 9 November 2023
Available online 10 November 2023
0257-8972/© 2023 The Authors. Published by Elsevier B.V. This is an open access article under the CC BY license (http://creativecommons.org/licenses/by/4.0/).

commonly selected [15,18]. This enhances the oxidation resistance significantly through the formation of a dense SiO_x-based scale. Similarly, for PVD synthesized TM-diboride thin films, Al- and Si-based alloying showed great potential in improving the high-temperature oxidation behavior [12,19]. Contrary to bulk materials, these concepts usually target the formation of AlB_2-structured solid solutions to maintain sufficiently high mechanical properties [20]. Glechner et al. [19,21,22] showed that Si alloying in transition metal diborides (TMB_2) increases the oxidation onset temperature by around 400 °C providing long-term oxidation resistance at 1200 °C for up to 100 h. Moreover, TiB_2 thin films alloyed with Al in [12] were investigated up to 800 °C, demonstrating a reduction in oxide scale growth by 75 % after isothermal annealing for 30 min. A particular disadvantage of solid-solution alloying routes is, however, the accompanying pore formation within the unaffected material upon extended oxidation periods, which is caused by the outward diffusion of the protective scale forming elements (*i.e.*, Al or Si) [19,20,23]. In order to avoid this chemical/microstructural separation, Wu et al. used a multilayered coating architecture of sputtered TiB_2 and Cr, achieving slightly improved low-temperature oxidation resistance up to 600 °C due to the direct supply of Cr to the coating surface [24].

Within this work, we suggest an alternative architectural approach consisting of a single protective thin film applied on top of TM-diboride base layers to drastically improve their long-term oxidation resistance. For this purpose, a matrix screening involving three TM-diborides (*i.e.*, WB_2, TiB_2, and HfB_2) and three Al- and/or Si-based top coatings (*i.e.*, Al-Si-N, Al-Si-O, and Si-O) is studied in detail.

2. Experimental

2.1. Deposition process

All coatings were deposited on single-crystalline ($1\bar{1}02$, 10 × 10 × 0.53 mm) and polycrystalline Al_2O_3 (20 × 7 × 0.38 mm) substrates, which were ultrasonically cleaned in acetone and ethanol for 10 min before all depositions. The coating process was conducted in two steps, starting with the synthesis of three different TM-diboride thin films, followed by the deposition of three different Al- and/or Si-based protective top layers. Overall, nine different coating architectures were investigated.

The synthesis of the TM-diboride thin films (*i.e.*, WB_2, TiB_2, or HfB_2) was performed in a laboratory-scale magnetron sputtering system using the corresponding 3-inch compound target (Plansee Composite Materials GmbH [25]). The targets were powered in direct current mode (DCMS) at around 4.8 W/cm^2 using Argon (purity of 99.999 %, Linde Gas GmbH) as a working gas. A base pressure below $3{\cdot}10^{-4}$ Pa was ensured before all depositions. Prior to the coating processes, the substrates were additionally cleaned through an Ar-ion etching step for 10 min, conducted at a total Ar pressure of 5 Pa and a substrate bias potential of −800 V. The target surface was further sputter-cleaned during the final 3 min of the Ar-etching sequence with a shutter placed between the target and substrate. The coating process was operated at a target-to-substrate distance of 90 mm at a constant substrate temperature of 550 °C. The substrates were placed in a rotating substrate holder (0.25 Hz) with a constant substrate bias potential of −40 V. The deposition pressure was maintained at 0.56 Pa. The coating times varied depending on the material system to obtain a consistent thickness of 2 μm, being 80 min for WB_2 and HfB_2, as well as 180 min for TiB_2.

An industrial-scale Oerlikon Balzers INNOVA system was used to deposit the Al- and/or Si-based top layers (*i.e.*, Al-Si-N, Al-Si-O, and Si-O) onto the TM-diboride thin films. For all top coatings a base pressure below 0.05 Pa was provided. The substrates were rotated using a two-fold rotating carousel. The chamber was heated to a substrate temperature of 450 °C for the deposition of the Si-O and Al-Si-N coatings, whereas a temperature of 550 °C was used to deposit the Al-Si-O top coating. To protect the TM-diboride thin films from immediate oxidation during the reactive deposition of Al-Si-O and Si-O as well as to achieve enhanced adhesion on the coating-coating interface, a 0.45 μm thick Si interlayer was introduced. The Si layer was deposited in a reactive process based on the Oerlikon Blazers central beam technology (average current of 120 A) using a mixture of silane and argon gas (90 sccm SiH_4, 80 sccm Ar, 99.999 % purity from Linde Gas GmbH). A bipolar substrate bias with a potential of ±40 V was utilized during the deposition.

The deposition conditions of the Si-O layer were analogous to the Si interlayer, however 180 sccm of O_2 were additionally introduced. The Al-Si-O and Al-Si-N top coatings were produced by reactive arc evaporation without the central beam technology using a pure Al target (purity of 99.5 %, Plansee Composite Materials GmbH) operated with a source current of 140 A. Si was added *via* SiH_4 gas at a flow rate of 50 sccm. A bipolar substrate bias potential of ±60 V was applied for the deposition of Al-Si-O, with again an oxygen flow rate of 180 sccm. Moreover, the Al-Si-N layer was synthesized using a bipolar substrate potential of ±40 V, with the nitrogen introduced at a constant pressure of 2 Pa. The deposition conditions of the individual top layers were determined in pre-studies on monolithic coatings.

2.2. Coating characterization

The chemical composition of the TM-diboride thin films was determined using inductively coupled plasma optical emission spectroscopy (ICP-OES) prior to the deposition of all top coatings. Details on the procedure can be found in Ref. [19]. Additionally, the chemical composition of the top layers was determined by standard-free energy dispersive X-ray spectroscopy (EDS) in top-view using a FEI Quanta 200 FEGSEM system at an acceleration voltage of 10.0 kV.

Cross-sectional characterization of the as-deposited coating architecture and growth morphology was performed by scanning electron microscopy (SEM) using a Zeiss Sigma 500 VO. Investigations of the thin films after oxidation treatments were conducted using a FEI Quanta 200 FEGSEM system. The fracture cross sections of all samples were investigated with an acceleration voltage of 5.0 kV to minimize charge build-up. Additionally, to examine the structure and pore formation of the oxidized coatings, focused ion beam (FIB) cross sections were prepared using a FIB-SEM dual beam system (ThermoFisher Scientific Scios 2). The cross sections were milled by a Ga^+ ion beam with currents ranging from 7 to 17 nA for fine milling, at an acceleration voltage of 30 kV.

Structural information as well as the phase composition of as-deposited and oxidized samples was obtained by X-ray diffraction (XRD) using a Panalytical X'Pert Pro MPD system operated in Bragg-Brentano geometry with Cu-K$_\alpha$ radiation (wavelength $\lambda = 1.5418$ Å).

To investigate the high-temperature behavior, dynamic oxidation tests in a mixture of synthetic air (50 ml/min) and helium protective gas (20 ml/min) were carried out in a combined DSC/TGA system (Netzsch STA 449 F1) equipped with a Rhodium furnace (TGA signals were processed only). The dynamic oxidation tests were performed from room temperature up to 1400 °C with a heating rate of 10 °C/min. Before each sample measurement, a baseline measurement was carried out with an empty crucible under equivalent conditions. The TGA data was recorded from coatings synthesized on pre-weighed polycrystalline Al_2O_3 substrates, which allowed for a precise measurement of the coating-only mass after the deposition process. Since the substrate material is inert in the investigated temperature range [19], any mass-change is directly related to oxidation/spallation/evaporation effects of the actual thin film material.

Additional long-term oxidation experiments up to 30 h were conducted in a conventional box furnace in ambient air at 1200 °C. The samples were placed directly into the preheated oven, removed from the high-temperature chamber after 30 h, and then allowed to cool to room temperature. Before these isothermal experiments, the adhesion between the TM-diboride and the protective layer was increased through vacuum annealing at 800 °C for 30 min. The annealing was conducted in

a CENTORR VI LF Series vacuum furnace at a heating rate of 20 °C/min and a base pressure below $1 \cdot 10^{-3}$ Pa.

Finally, transmission electron microscopy (TEM) of two selected samples was performed to investigate the oxide-scale formation and coating architecture after long-term oxidation treatments using a FEI TECNAI F20 (S)TEM system (operated at 200 kV acceleration voltage). Selected area electron diffraction (SAED) images were taken for crystallographic analysis. The TEM lamellae were prepared *via* a standardized focused ion beam (FIB) lift out procedure on a ThermoFisher Scios II. The local chemical composition was further determined by electron energy loss spectroscopy (EELS). The EELS data was quantified using the Digital Micrograph software package (Gatan Microscopy Suite, version 3.22).

3. Results and discussion

In Fig. 1 the architectural design of the three different TM-diborides (TM = W, Ti, Hf, blue layer) in combination with the three different protective top layers is summarized (yellow layer). As mentioned above, an intermediate Si layer was introduced for the oxide-based top layers to prevent *in-situ* oxidation of the diboride thin films during the reactive deposition process, as well as to improve adhesion (see Fig. 1, orange layer). The following sections contain a comprehensive analysis of all sample configurations with respect to their growth morphology and oxidation resistance in high-temperature oxidative environments.

3.1. Chemical composition & growth morphology

The chemical composition of the TM-diborides was determined by ICP-OES, revealing a slight boron deficiency for the $WB_{1.9}$ layer, while both the $TiB_{2.7}$ and $HfB_{2.4}$ thin films contain excess boron. Hence, it can be expected that especially the latter two variants exhibit boron-enriched grain boundary sites – typically susceptible to B_2O_3 volatilization [26,27]. These deviations from the stoichiometric TMB_2 structure in the target materials originate from different scattering angles and mass ratios between the involved species, as previously detailed by Neidhardt et al. [20,26,28]. Additionally, the chemical composition of the top layer was determined using standard-free EDS, which resulted in an Al-Si-N layer composition of $Al_{0.20}Si_{0.15}N_{0.65}$, an Al-Si-O composition of $Al_{0.22}Si_{0.09}O_{0.69}$, and a Si-O composition of $Si_{0.22}O_{0.78}$. For further use in the text, the abbreviated form (*i.e.*, Al-Si-N, Al-Si-O, and Si-O) is used.

In Fig. 2 the SEM fracture cross sections of all coating configurations are shown in the as-deposited state. The layered structure is indicated with colored dashed lines on the left side of each image as a guide to the eye. The single-crystalline Al_2O_3 substrate is followed by the TM-diboride layer ($WB_{1.9}$ in Fig. 2a-c, $TiB_{2.7}$ in Fig. 2d-f, and $HfB_{2.4}$ in Fig. 2g-i), a Si interlayer (only present for Al-Si-O and Si-O top layers) and the protective surface layers (Al-Si-N in the left column, Al-Si-O in the center column, and Si-O in the right column).

All TMB_2 coatings show a dense and rather featureless morphology. $TiB_{2.7}$ exhibits slight indications for a columnar morphology in top most regions. The average thickness of the TM-diboride films was determined with 2.3, 1.7, and 1.8 µm for $WB_{1.9}$, $TiB_{2.7}$, and $HfB_{2.4}$, respectively. The Si interlayer introduced for all samples with Al-Si-O and Si-O top layers were grown to a thickness of ~450 nm. Moreover, the different protective top layers were determined with an average thickness of 4.5, 3.6, and 4.8 µm for Al-Si-N, Al-Si-O, and Si-O, respectively. The top coatings further appear as homogenous and dense without any texture on all TM-diboride thin films. In contrast to the $TiB_{2.7}$ and $HfB_{2.4}$ thin films, pores can be observed at the coating-coating interface between the Al-Si-N and $WB_{1.9}$ coating, indicating poor layer adhesion. In addition, due to the arc evaporation process from elemental Al targets, both the Al-Si-N and Al-Si-O coatings contain metallic macro particles which contribute to increased surface roughness.

3.2. Phase formation

The phase formation of each layer during the successive deposition stages was investigated by X-ray diffraction in Bragg-Brentano geometry, as presented in Fig. 3. The diffractograms are grouped according to the TM-diboride base layer, with the data in Fig. 3a corresponding to $WB_{1.9}$, in Fig. 3b to $TiB_{2.7}$, and in Fig. 3c to $HfB_{2.4}$, respectively. In addition, each subfigure is arranged from bottom to top, starting with the bare TM-diboride followed by the samples having an additional Al-Si-N, Si/Al-Si-O, or Si/Si-O top coating. All TM-diborides were synthesized as single-phased, α-TMB_2-structured (AlB_2 prototype) thin films. In particular, $WB_{1.9}$ and $TiB_{2.7}$ exhibit a clearly preferred (001) growth orientation. Contrary, the $HfB_{2.4}$ containing samples reveal a polycrystalline grain orientation. Both sample configurations with the Si interlayer further contain diffraction peaks corresponding to pure Si, suggesting that the Si interlayer is in a partly crystalline state.

However, the most striking observation in the diffractograms is that irrespective of the TM-diboride, all protective top layer variants were deposited in a fully X-ray amorphous state, as suggested by the lack of additional diffraction peaks. Solely two reflexes indicative of metallic Al [29] are observed for the samples containing Al-Si-N and Si/Al-Si-O top coatings. Following the SEM fracture cross section in Fig. 2, these peaks can be assigned to Al-rich macro-particles formed during the arc evaporation process.

3.3. Dynamic oxidation

The oxidation behavior of all coating variants including the bare TMB_2 thin films without protective top layer was investigated by dynamic oxidation experiments in synthetic air up to 1400 °C (10 °C/min heating rate). Fig. 4 presents the mass change of the coating material normalized to the coated area as function of the temperature. Please note, that the inert substrate material does not contribute to the recorded mass signal.

The reference measurements of the bare TMB_2 thin films clearly highlight the necessity for additional measures to sustain these materials in oxygen containing environments at elevated temperatures. While $WB_{1.9}$ and $TiB_{2.7}$ reveal a similar oxidation onset temperature of about 500 °C (see Fig. 4a-b), $HfB_{2.4}$ is able to tolerate temperatures between

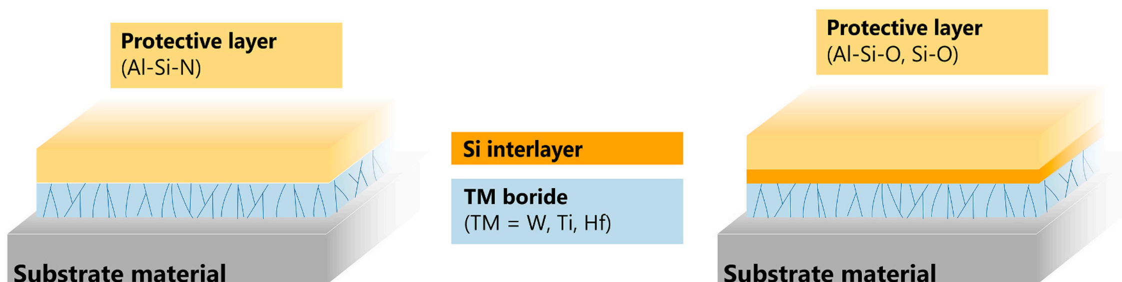

Fig. 1. Architectural design preserving $TMB_{2\pm z}$ coatings against high-temperature oxidation by introducing different protective top layers. The Si interlayer is solely present for Al-Si-O and Si-O top layers.

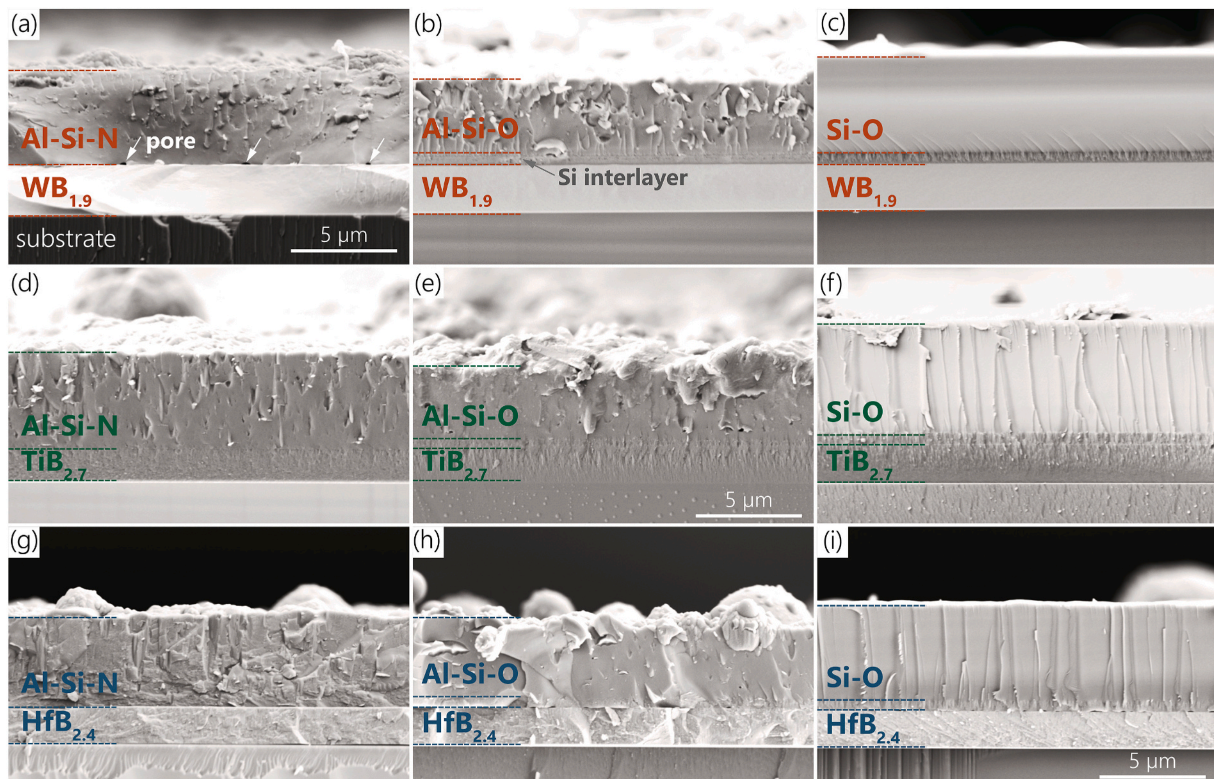

Fig. 2. SEM fracture cross sections of the as-deposited coatings on single-crystalline Al_2O_3 substrate. The upper image row depicts the $WB_{1.9}$-based thin films with an (a) Al-Si-N, (b) Al-Si-O, and (c) Si-O protective top layer. The center and bottom image rows display the same top layer sequence for (d-f) $TiB_{2.7}$ and (g-i) $HfB_{2.4}$ thin films, respectively. White arrows in (a) indicate small pores at the interface between the Al-Si-N and the $WB_{1.9}$ layer. An additional Si interlayer (as exemplarily marked in (b)) is present for all Al-Si-O and Si-O top layers.

700 and 750 °C before noticable mass gain is recorded (see Fig. 4c). The data confirms that the bare diboride materials (irrespective of the stoichiometry) are incapable of forming protective oxide scales, with the coating mass increasing to a respective maxima between 900 and 1200 °C. At temperatures beyond 1200 °C all TMB_2 thin films show a decreasing mass signal, which correlates to the volatilization of B_2O_3 [16,19].

Adding a protective Al-Si-N top coating to the TMB_2 thin films results in increased oxidation resistance for all samples, visible in a pronounced shift of the oxidation onset temperature to the range between 800 and 1000 °C. Interestingly, not only the oxidation onset temperature varies between the samples, also the recorded oxidation kinetics are markedly different. While the Al-Si-N coating on $WB_{1.9}$ suffers from accelerated mass gain – even exceeding the $WB_{1.9}$ reference data above 950 °C (see Fig. 4a) – the identical coating on $TiB_{2.7}$ and $HfB_{2.4}$ allows for enhanced oxidation resistance up to ~1000 °C before continued oxide scale growth is observed (see Fig. 4b-c). This drastic oxidation of the Al-Si-N on top of $WB_{1.9}$ is suggested to be caused by any unobserved microstructural defect/feature causing this kind of break away oxidation. The variations in CTE values (α_a and α_c, with a and c standing for the different crystallographic directions within the hexagonal system) among the three different diborides concerning the Al_2O_3 substrate may also play a role in the observed discrepancies in the oxidation kinetics. Considering theses distinctions (WB_2: $6.0 \cdot 10^{-6}$ and $9.4 \cdot 10^{-6}$ K^{-1} at 300 K for α_a and α_c, respectively; TiB_2: $5.9 \cdot 10^{-6}$ and $8.5 \cdot 10^{-6}$ K^{-1} at 300 K for α_a and α_c, respectively; HfB_2: $5.2 \cdot 10^{-6}$ and $6.0 \cdot 10^{-6}$ K^{-1} at 300 K for α_a and α_c, respectively [30,31]; Al_2O_3: $7 \cdot 10^{-6}$ K^{-1} at 300 K [32]), it is reasonable that WB_2 exhibits the least favorable substrate adhesion. Furthermore, the difference between the top layers/Si and the diborides also influence the behavior (Si: $2.6 \cdot 10^{-6}$ K^{-1} at 300 K [33]; AlN: $4.2 \cdot 10^{-6}$ and $5.3 \cdot 10^{-6}$ K^{-1} at 300 K for α_a and α_c, respectively [34]; Al-Si-O (mullite): 4–$6 \cdot 10^{-6}$ K^{-1} at 300 K [35,36]; SiO_2: $0.6 \cdot 10^{-6}$ K^{-1} at 300 K [37]). In addition, the small pores at the interface further supports rapid scale formation of the underlying boride, see cross section in Fig. 2a. Moreover, the Al-Si-N protected $TiB_{2.7}$ reveals a step-wise oxidation behavior with a stable mass plateau of ~0.10 mg/cm^2 between 850 and 1050 °C (see Fig. 4b), suggesting the temporary formation of a stable oxide scale prior to a full oxidation of the remaining coating material. In general, the step-wise oxidation is a combined process of an initial oxidation and a subsequent break away phenomenon. The general difference in oxidation behavior between these samples may be seen in varying growth morphologies of the Al-Si-N coating – note the absence of a uniform interlayer in the architecture – as well as from differences in thermal expansion to the base TMB_2 coatings. Overall, the dynamic oxidation tests involving Al-Si-N protective top layers did not result in the formation of a sufficient oxygen barrier above 1000 °C, hence these sample configurations were excluded from the following isothermal oxidation treatments (see Section 3.4).

In clear contrast to the Al-Si-N coated TMB_2 samples, both the Si/Al-Si-O and Si/Si-O coatings enable outstanding oxidation resistance irrespective of the diboride base layer, as indicated by negligible mass gain/loss over the entire temperature range. In detail, thin films with a protective Si/Al-Si-O top layer experience a total mass gain between 0.05 and 0.07 mg/cm^2, particularly in the temperature range above 1150 °C. This performance is even exceeded by Si/Si-O coated samples, which reveal a maximum mass change of 0.02 mg/cm^2. These results suggest that both protection layer concepts provide a stable, dense scale formation which prevents a continued and fast oxygen inward diffusion towards the unaffected coating material.

3.4. *Isothermal oxidation*

The long-term performance of the Si/Al-Si-O and Si/Si-O top coatings was further assessed by isothermal oxidation tests at 1200 °C for 3

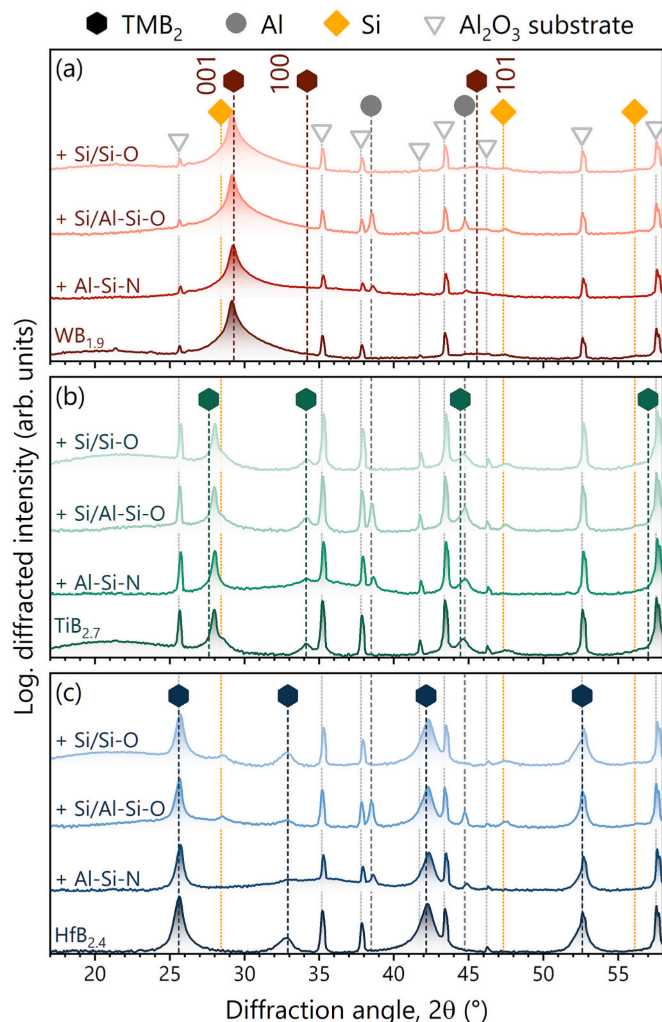

Fig. 3. X-ray diffractograms of all samples with (a) $WB_{1.9}$ (red hexagon, α-structure, [38]), (b) $TiB_{2.7}$ (green hexagon, α-structure, [39]), or (c) $HfB_{2.4}$ (blue hexagon, α-structure, [40]) coating as base layer. Each subfigure is arranged from bottom to top, starting with the pure TM-diboride coating followed by sample configurations with additional Al-Si-N, Si/Al-Si-O, or Si/Si-O top coating. All measurements were performed on coated polycrystalline Al_2O_3 substrates (light-grey triangle, [41]) in Bragg-Brentano geometry. Additional diffraction peaks correspond to metallic Al (dark grey circle, [29]) and Si (yellow diamond, [42]). (For interpretation of the references to colour in this figure legend, the reader is referred to the web version of this article.)

and 30 h in lab-air conditions, respectively. The resulting oxide scale formation was then investigated by cross-sectional microscopy analysis and in terms of phase formation by X-ray diffraction. Prior to these tests, vacuum annealing treatments were performed for 30 min at 800 °C to improve the adhesion of the Si interlayer to the TM-diboride as well as the protective top coating. This pretreatment was performed to minimize spallation of the oxide scale during sample cooling from 1200 °C. However, the oxidized $WB_{1.9}$-based samples were found to have fully delaminated from the polycrystalline Al_2O_3 substrates for both oxidation periods, indicating limited adhesion under the tested conditions and thus preventing further investigations. It should be noted, that WB_2 has the largest discrepancy of the CTE values in the c-axis direction, which may contribute to the observed delamination.

Fig. 5 displays the SEM fracture cross sections of all oxidized samples with a $TiB_{2.7}$ base layer. The upper image row (see Fig. 5a-c) corresponds to the Si/Al-Si-O top coating, whereas the bottom image row (see Fig. 5d-f) contains the Si/Si-O protected samples. From left-to-right the images are aligned with increasing duration of the oxidation treatment.

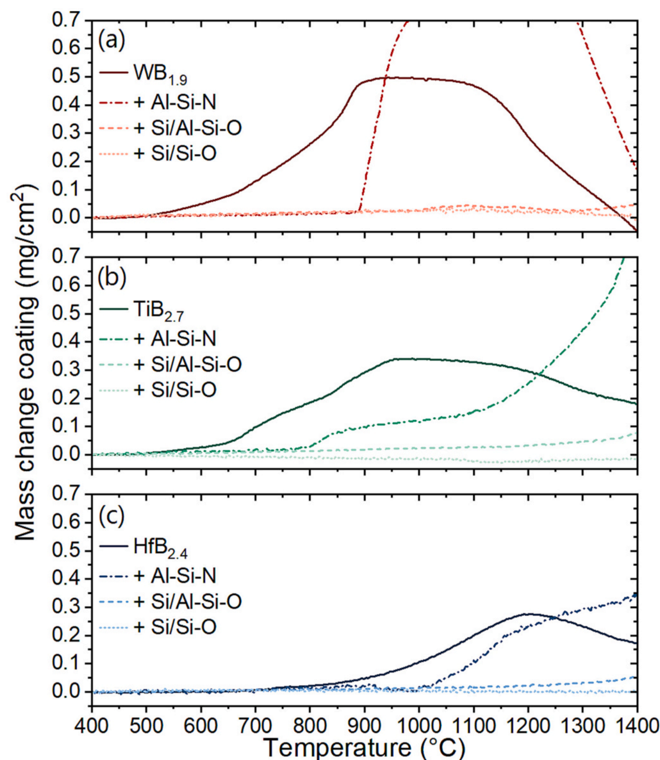

Fig. 4. Thermogravimetric analysis of the coating mass during dynamic oxidation up to 1400 °C in synthetic air. The data is grouped into (a) $WB_{1.9}$, (b) $TiB_{2.7}$, and (c) $HfB_{2.4}$ based coatings, with each section containing reference data of the bare TMB_2 thin film as well as with the three top layer variants Al-Si-N, Si/Al-Si-O, and Si/Si-O.

After 3 h of isothermal oxidation (see Fig. 5a-b), the protective Si/Al-Si-O layer exhibits a significant change in morphology. The protective coating shows increased porosity – in particular within the Si interlayer – and a pronounced increase in surface roughness when compared to the as-deposited state. The underlying $TiB_{2.7}$ coating, however, visually remains unchanged after the first annealing treatment. Furthermore, adhesion to the polycrystalline Al_2O_3 substrate appears to be intact. After 30 h oxidation at 1200 °C (see Fig. 5c), the pore formation within the Si interlayer progresses, whereas porosity in the Al-Si-O top coating appears reduced. Additional visual information is provided by FIB cross sections in the supplementary part (see Fig. S1), highlighting that fractured cross sections (as presented) in Fig. 5 also depend on the crack path compared to the FIB milled ones – obtaining a more continuous trend in scale thickness and pore formation.

Fig. 6a contains the corresponding X-Ray diffractograms, arranged from bottom to top with increasing oxidation time. The data recorded after 3 h already indicates the formation of several crystalline structures within the protective coating architecture. Comparison to standardized reference patterns suggests that the Al-Si-O coating crystallizes into an $3Al_2O_3 \cdot 2SiO_2$ mullite-based structure. In addition, the presence of both tetragonal and hexagonal SiO_2 as well as hints for a TiO_2 phase are observed. Also, the partly amorphous Si interlayer crystallizes at this temperature range. After 30 h, the intensity of all diffraction peaks including that of TiB_2 increases, suggesting continued crystallization and grain growth. Overall, the presence of the TiB_2 phase after the oxidation treatment shows the oxygen barrier capabilities of the protective layer concept.

The SEM images in Fig. 5d-f show $TiB_{2.7}$ coatings protected by Si/Si-O. The top coating has a dense, featureless morphology in the as-deposited state (see Fig. 5d), which is maintained throughout the oxidation treatment (see Fig. 5e-f). Moreover, the coating surface remains significantly smoother than for Si/Al-Si-O coated samples after

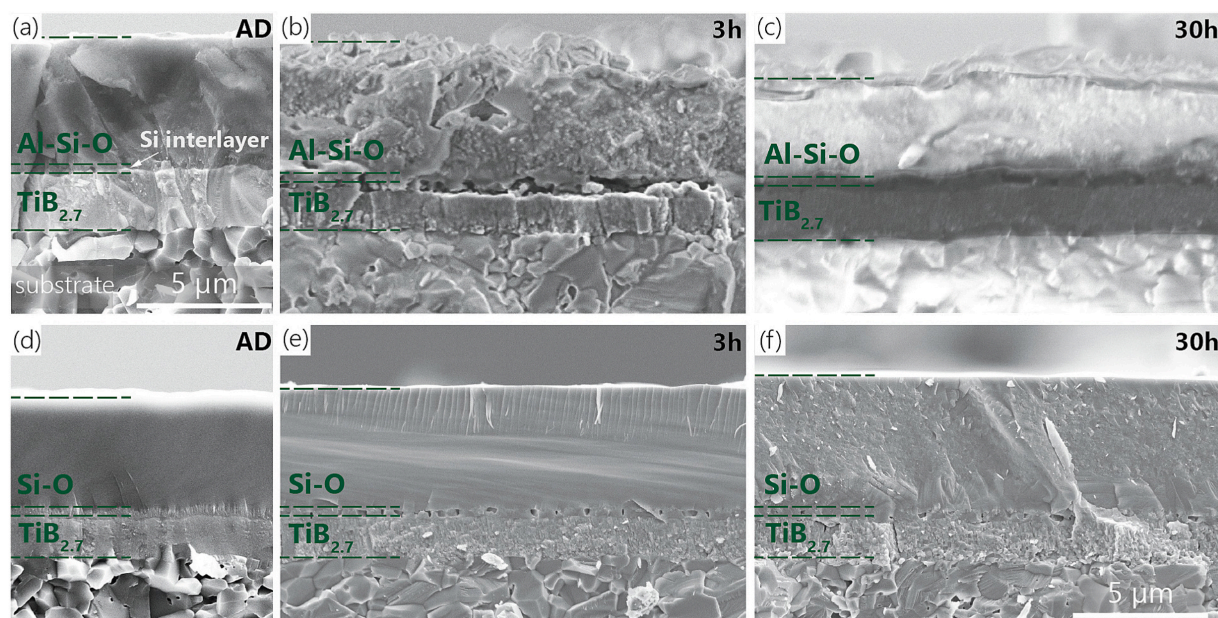

Fig. 5. SEM fracture cross sections of $TiB_{2.7}$ thin films protected with (a-c) Si/Al-Si-O and (d-f) Si/Si-O top coatings. (a) and (d) show the as-deposited state for reference (AD), (b) and (e) after 3 h, (c) and (f) after 30 h of isothermal oxidation at 1200 °C in ambient air. All images were recorded on coated polycrystalline Al_2O_3 substrates.

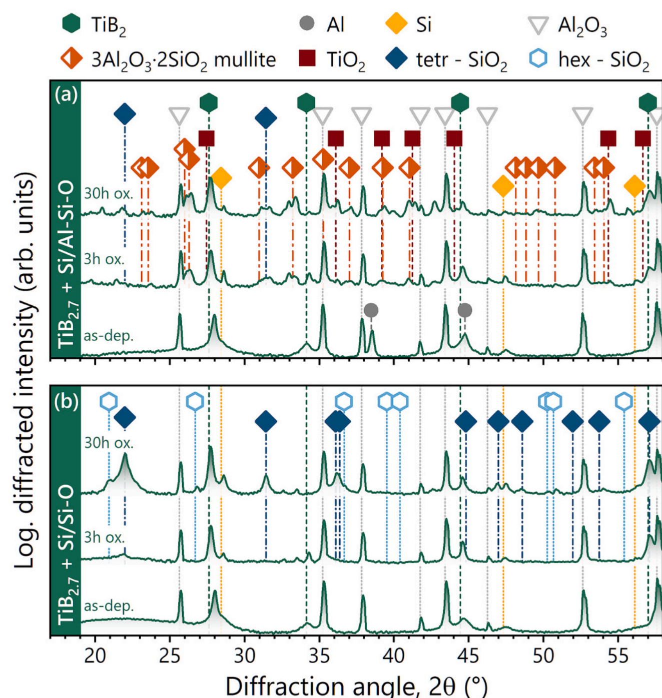

Fig. 6. XRD diffractographs of $TiB_{2.7}$ thin films protected with (a) Si/Al-Si-O and (b) Si/Si-O top coatings. In each group, the lower diffractograph represents the as-deposited state, followed by the data recorded after 3 and 30 h of isothermal oxidation at 1200 °C in ambient air, respectively. The data was collected from coated polycrystalline Al_2O_3 substrates (grey triangles, [41]). The following standardized reference patterns are included: hexagonal TiB_2 (green hexagon, α-structure, [39]), cubic Al (grey circle, [29]), cubic Si (yellow diamond, [42]), orthorhombic $3Al_2O_3{\cdot}2SiO_2$ (mullite, half-filled, orange diamond, [43]), tetragonal TiO_2 (dark red cube, [44]), tetragonal SiO_2 (blue diamond, [45]) and hexagonal SiO_2 (light blue, open hexagon, [46]). (For interpretation of the references to colour in this figure legend, the reader is referred to the web version of this article.)

oxidation. The data further shows that after 3 and 30 h, the Si interlayer exhibits initial signs of pore formation – indicative of accelerated diffusion processes – while the $TiB_{2.7}$ coating maintains a dense morphology throughout the full oxidation treatment. Overall, good adhesion between the individual layers is still recorded after 30 h at 1200 °C (see Fig. 5f), underlining the excellent protective character of the Si-O based top coat. The respective XRD data in Fig. 6b again shows the (re-)crystallization of all individual layers, with the initially amorphous Si/Si-O coating transforming into tetragonal- and hexagonal-structured SiO_2 next to the recrystallized Si interlayer after 3 and 30 h at 1200 °C, respectively.

Fig. 7 shows SEM fracture cross sections of the $HfB_{2.4}$-based coating architectures after identical isothermal oxidation treatments at 1200 °C for up to 30 h in ambient air. Following the arrangement of Fig. 5, all images corresponding to $HfB_{2.4}$ protected by Si/Al-Si-O top coatings are given in Fig. 7a-c, whereas the Si/Si-O coated samples are displayed in Fig. 7d-f. Moreover, from left-to-right the images refer to increasing durations of the oxidation treatment.

After 3 h of annealing at 1200 °C, $HfB_{2.4}$ protected by Si/Al-Si-O (see Fig. 7b), exhibits a more textured and granular morphology throughout all layers. In addition, the top surface of the protective Al-Si-O layer shows a pronounced increase in surface roughness. After 30 h of annealing (see Fig. 7c), all layers obtained a globular morphology with small pores formed throughout the $HfB_{2.4}$ as well as the Al-Si-O coating close to the Si interlayer. Additional visual support is provided by FIB cross sections, see Fig. S2 in the supplementary part. Nevertheless, the initial layered structure is distinctly maintained and the layer adhesion between the polycrystalline Al_2O_3 substrate and the subsequent layers is still given.

Similar to the $TiB_{2.7}$-based coating, the corresponding X-ray diffractograms in Fig. 8a reveal the formation of a crystalline $3Al_2O_3{\cdot}2SiO_2$ mullite phase after 3 and 30 h of isothermal annealing. Moreover, both the tetragonal- and hexagonal-structured variants of SiO_2 are formed next to hints for a monoclinic HfO_2 phase. Still, the hexagonal $HfB_{2.4}$ phase is well present after the entire annealing treatment, suggesting a recrystallization due to decreasing peak-width.

The final configuration of $HfB_{2.4}$ protected by a Si/Si-O coating is studied before and after oxidation in Fig. 7d-f. Analogous to the $TiB_{2.7}$-based coatings, both the Si-O and the TM-diboride layer maintain a

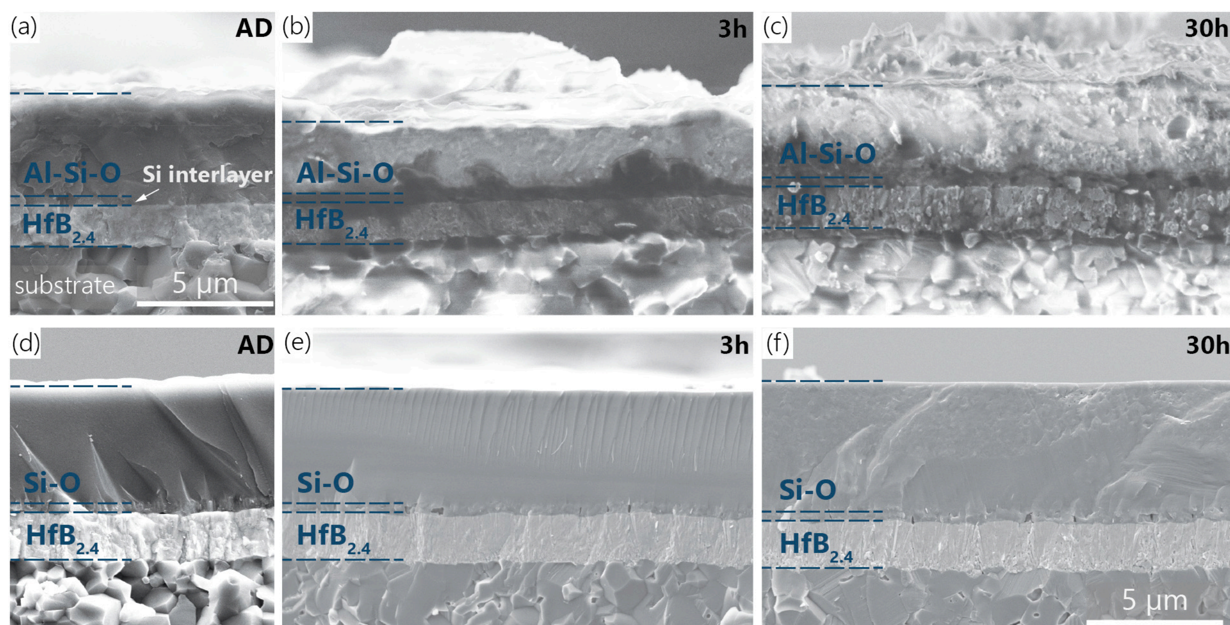

Fig. 7. SEM fracture cross sections of $HfB_{2.4}$ thin films protected with (a-c) Si/Al-Si-O and (d-f) Si/Si-O top coatings. (a) and (d) show the as-deposited state for reference (AD), (b) and (e) after 3 h, (c) and (f) after 30 h of isothermal oxidation at 1200 °C in ambient air. All images were recorded on coated polycrystalline Al_2O_3 substrates.

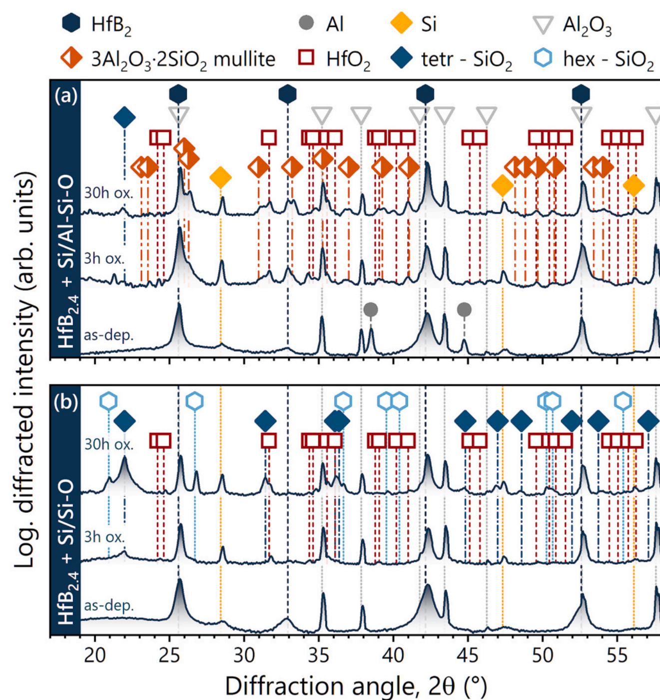

Fig. 8. XRD diffractographs of $HfB_{2.4}$ thin films protected with (a) Si/Al-Si-O and (b) Si/Si-O top coating. In each group, the lower diffractograph represents the as-deposited state, followed by the data recorded after 3 and 30 h of isothermal oxidation at 1200 °C in ambient air, respectively. The data was collected from coated polycrystalline Al_2O_3 substrates (grey triangles, [41]). The following standardized reference patterns are included: hexagonal HfB_2 (blue hexagon, α-structure, [40]), cubic Al (grey circle, [29]), cubic Si (yellow diamond, [42]), orthorhombic $3Al_2O_3{\cdot}2SiO_2$ (mullite, half-filled, orange diamond, [43]), monoclinic HfO_2 (dark red cube, [47]), tetragonal SiO_2 (blue diamond, [45]) and hexagonal SiO_2 (light blue, open hexagon, [46]). (For interpretation of the references to colour in this figure legend, the reader is referred to the web version of this article.)

highly dense morphology even after 30 h of annealing at 1200 °C. The porosity within the Si interlayer appears less pronounced, with excellent adhesion recorded for all layers.

Looking at the phase formation in Fig. 8b, next to an intact and recrystallized $HfB_{2.4}$ phase, again the formation of tetragonal and hexagonal SiO_2 is observed. In addition, the monoclinic HfO_2 structure appears to contribute to the excellent oxidation resistance observed for this coating architecture.

3.5. *Scale formation on $HfB_{2.4}$ at 1200 °C*

Based on the previously discussed dynamic and isothermal oxidation treatments, both the Si/Al-Si-O and Si/Si-O protective coatings showed exceptional high-temperature oxidation resistance up to 1200 °C on $TiB_{2.7}$ and $HfB_{2.4}$. In particular, the $HfB_{2.4}$ samples excelled with an intact layer structure, exceptional layer adhesion and a dense microstructure – especially within the Si interlayer – after annealing for 30 h in air at 1200 °C. Therefore, a more detailed investigation on the scale growth, chemical distribution, and microstructure was conducted on oxidized $HfB_{2.4}$ coatings with Si/Al-Si-O and Si/Si-O protective top coatings.

Fig. 9a shows a bright-field TEM micrograph of the $HfB_{2.4}$-Si/Al-Si-O coating architecture after 30 h of isothermal oxidation at 1200 °C. As suggested by the X-ray diffraction data (see Fig. 8a), large globular grains within the $HfB_{2.4}$ base layer confirm a recrystallization of the material, however, hardly any pores are visible within the diboride coating. The image also shows a perfectly continuous adhesion of the recrystallized Si interlayer to the $HfB_{2.4}$ and Al-Si-O coatings. Moreover, in agreement with previous SEM fracture cross sections (see Fig. 5a-c), the nanostructured protective top layer appears as rough and slightly porous, with large inclusions holding pure Si as determined by localized EDS analysis. The observed structure is strongly connected to the crystallization of the complex orthorhombic $3Al_2O_3{\cdot}2SiO_2$ mullite phase from the initially amorphous coating (compare with Fig. 8a).

To get an insight into the diffusion processes after annealing in the high-temperature regime, an EELS line-scan was recorded covering the entire coating architecture. In Fig. 9a the position and direction of the line-scan is indicated by a blue arrow. The chemical distribution

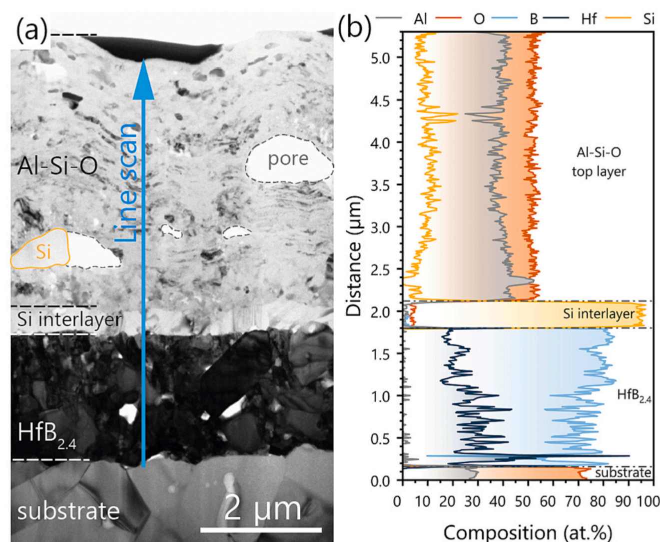

Fig. 9. TEM analysis of an oxidized $HfB_{2.4}$ thin film protected with an Al-Si-O top coating. The sample was annealed in ambient air at 1200 °C for 30 h. (a) Bright-field image of the sample cross section showing the polycrystalline Al_2O_3 substrate, the $HfB_{2.4}$ base layer, the Si interlayer, as well as the Al-Si-O protective coating from bottom to top. The blue arrow in (a) indicates the position and direction of the (b) EELS line-scan. (For interpretation of the references to colour in this figure legend, the reader is referred to the web version of this article.)

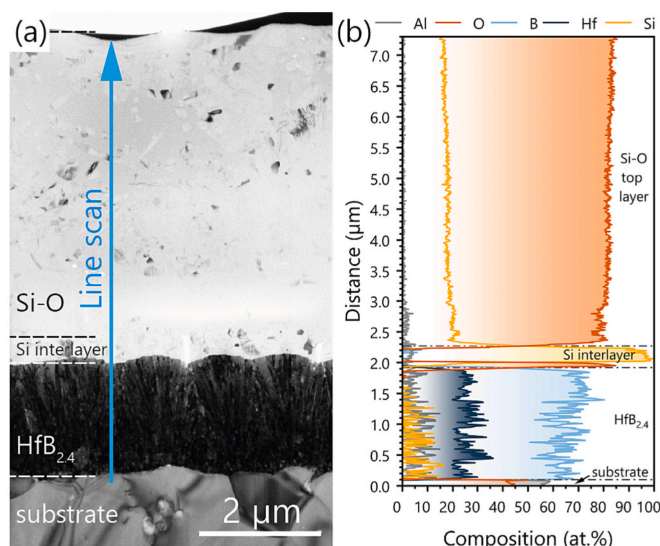

Fig. 10. TEM analysis of an oxidized $HfB_{2.4}$ thin film protected with a Si-O top coating. The sample was annealed in ambient air at 1200 °C for 30 h. (a) Bright-field image of the sample cross section showing the polycrystalline Al_2O_3 substrate, the $HfB_{2.4}$ base layer, the Si interlayer, as well as the Si-O protective coating from bottom to top. The blue arrow in (a) indicates the position and direction of the (b) EELS line-scan. (For interpretation of the references to colour in this figure legend, the reader is referred to the web version of this article.)

underlines an intact, layered structure after annealing at 1200 °C, with the individual coatings fully separated from each other. Hf appears to be slightly depleted towards the Si interlayer, with an average concentration of 30 at.% recorded close to the substrate near interface (note the close correlation with the chemistry determined by ICP-OES). Moreover, the HfO_2 observed during X-ray diffraction could not be identified in this localized analysis.

Furthermore, the line-scan shows a clear demarcation of the $HfB_{2.4}$ layer from the substrate and the adjacent Si interlayer. The absence of interdiffusion between HfB_2 and Si is in good correlation with previous works, where limited solubility was determined for Si in TMB_2 thin films, leading to a chemical separation upon thermal annealing [20,22]. Interestingly, the Al-Si-O-based protective layer shows pronounced porosity within the crystallized Al_2O_3-SiO_2 matrix. The pores are partly filled with Si, pointing towards excess Si (see Fig. 9b) within the mullite scale which subsequently concentrates in distinct locations.

Nevertheless, it can be stated that the selected coating system shows excellent oxidation resistance, tested at 1200 °C for up to 30 h. The oxygen diffusion into the diboride coating is fully suppressed, with only minor concentration detected within the Si interlayer. Hence, it can be concluded that the Al-Si-O layer served as a good protective barrier against oxygen at the tested conditions.

The bright-field image in Fig. 10a depicts the cross-sectional morphology of a $HfB_{2.4}$ thin film protected by a Si/Si-O top coating during 30 h of isothermal oxidation at 1200 °C. In contrast to the pronounced recrystallization of the diboride coating in Fig. 9a, the $HfB_{2.4}$ coating maintained a fine columnar morphology, typical for sputter-deposited thin films. Furthermore, the entire coating architecture appears as dense without noticeable pores in the microstructure or between the individual layers. Contrary to the Al-Si-O based top layer, the Si-O coating remained mostly amorphous with small SiO_2 crystallites embedded in the matrix.

As for the previously described sample with Al-Si-O top coating, an EELS line scan was recorded for $HfB_{2.4}$ protected with Si-O. Irrespective of the relative low Si solubility in TM diborides, a Si diffusion of about 5–10 at. % into the diboride layer can be indicated, which could possibly be the reason for inhibiting the recrystallization of the $HfB_{2.4}$ layer during the oxidation process. This is a highly interesting observation, as Si typically tends to separate within HfB_2 structures [22]. The ratio between B to Hf is nearly constant over the entire thickness of the diboride layer. At the interface to the Si layer, a very narrow O peak is visible, that may indicate a pore. Nevertheless, this layer also impressively withstood the challenging oxidative environment at 1200 °C since the diboride thin film remained entirely unaffected by O.

4. Conclusions

In this study, an effective architectural design is demonstrated to protect TM-diboride coatings against high-temperature oxidation. Reactively grown Al-Si-N, Al-Si-O, and Si-O top layer provide long-term stability for oxidation sensitive binary diborides up to 1200 °C. These architectural designs were applied to sputter deposited $WB_{1.9}$, $TiB_{2.7}$, and $HfB_{2.4}$ thin films. A pure Si adhesion layer was introduced to prevent *in-situ* oxidation during the synthesis of the oxide based top layers.

- Structural analysis of the as deposited coatings showed α-structured diborides in the base layers and X-ray amorphous top layers. The introduced Si adhesion layer obtained a crystalline character.
- During thermo-gravimetric screening up to 1400 °C, the Al-Si-N protective layers exhibited accelerated mass gain beyond 800–1000 °C, while Si-O and Al-Si-O experienced significantly fewer mass changes.
- In long-term isothermal oxidation tests as 1200 °C for 3 and 30 h, the $WB_{1.9}$ architectures delaminated. In contrast, the $TiB_{2.7}$ and $HfB_{2.4}$ thin films, protected by Al-Si-O and Si-O, maintained their layered structures even after 30 h.
- Detailed microstructural analysis of the $HfB_{2.4}$ based architectures confirmed the outstanding oxidation resistance, with no oxygen inward diffusion beyond the Si adhesion layer. The Al-Si-O layer on $HfB_{2.4}$ displayed more pronounced diffusion processes, forming a phase-separated Al_2O_3-SiO_2 scale. Additionally, the underlying $HfB_{2.4}$ was strongly recrystallized. In contrast, the fully dense Si-O

protective layer showed no pores, and the $HfB_{2.4}$ base layer remained unaffected.

CRediT authorship contribution statement

S. Richter: Conceptualization, Investigation, Data Analysis, Writing, Visualization, – original draft, **T. Glechner**: Conceptualization, Investigation, **T. Wojcik**: Investigation, **B. Widrig**: Investigation, **S. Kolozsvári**: Project Administration, Writing – Review & Editing, **P. Polcik**: Project Administration, Writing – Review & Editing, **O. Hunold**: Project Administration, Writing – Review & Editing, **L. Zauner**: Conceptualization, Data Analysis, Visualization, Writing – Review & Editing, **J. Ramm**: Conceptualization, Project Administration, Writing – Review & Editing, **H. Riedl**: Supervision, Conceptualization, Project Administration, Writing – Review & Editing.

Declaration of competing interest

The authors declare that they have no known competing financial interests or personal relationships that could have appeared to influence the work reported in this paper.

Data availability

Data will be made available on request.

Acknowledgments

The financial support by the Austrian Federal Ministry for Digital and Economic Affairs, the National Foundation for Research, Technology and Development and the Christian Doppler Research Association is gratefully acknowledged (Christian Doppler Laboratory "Surface Engineering of high-performance Components"). We also thank Plansee SE, Plansee Composite Materials GmbH, and Oerlikon Balzers, Oerlikon Surface Solutions AG for financial support. We also thank the X-ray center (XRC) of TU Wien for beam time and the electron microscopy center - USTEM TU Wien - for using the SEM and TEM facilities. Finally, we acknowledge TU Wien Bibliothek for financial support through its Open Access Funding Programme.

Appendix A

In addition, FIB cross sections were prepared of the samples oxidized at 1200 °C for 3 and 30 h in ambient air. In Fig. S1 as well as in Fig. S2, the layered structure consisting of TM diboride, Si interlayer and the two top coatings (Al-Si-O and Si-O) can be clearly seen, even after oxidation. The top layers are overexposed due to charging during imaging.

Based on the FIB cross sections, there is a clear tendency for the layer thickness to increase with increasing oxidation time. For the Al-Si-O top layer, more pronounced pore formation can be seen in (b–c) in both Fig. S1 and Fig. S2, which is partly due to phase transformation into the mullite structure $3Al_2O_3{\cdot}2SiO_2$. However, for the Si-O protected coatings, less pore formation is evident. In the oxidized state after 30 h, see (f) in Fig. S1 and Fig. S2, SiO_2 crystals are embedded in an amorphous Si-O matrix, which was verified by XRD and TEM investigations.

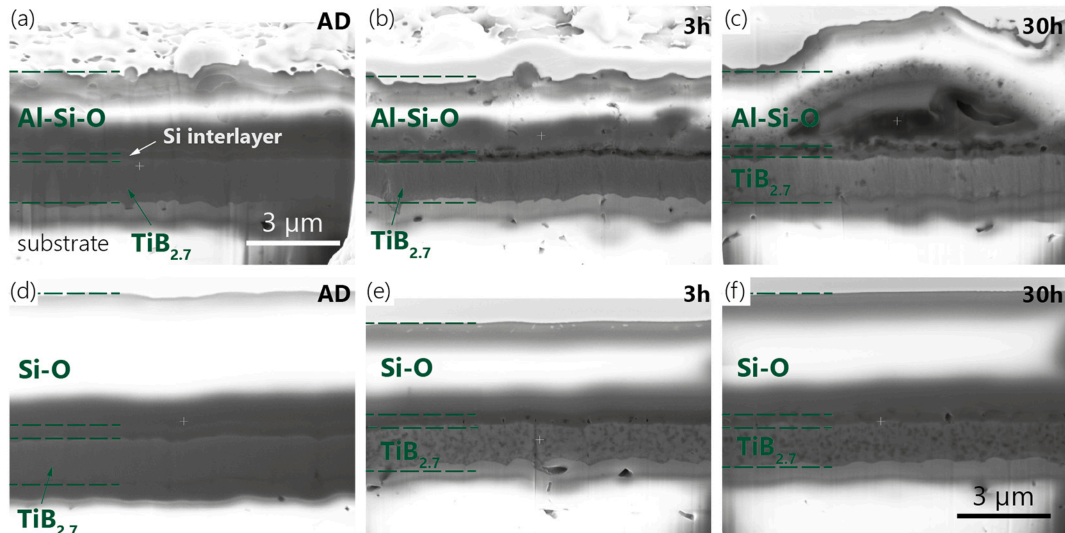

Fig. S1. FIB cross sections of $TiB_{2.7}$ thin films protected with (a–c) Si/Al-Si-O and (d–f) Si/Si-O top coatings. (a) and (d) show the as-deposited state for reference (AD), (b) and (e) after 3 h, (c) and (f) after 30 h of isothermal oxidation at 1200 °C in ambient air. All images were recorded on coated polycrystalline Al_2O_3 substrates.

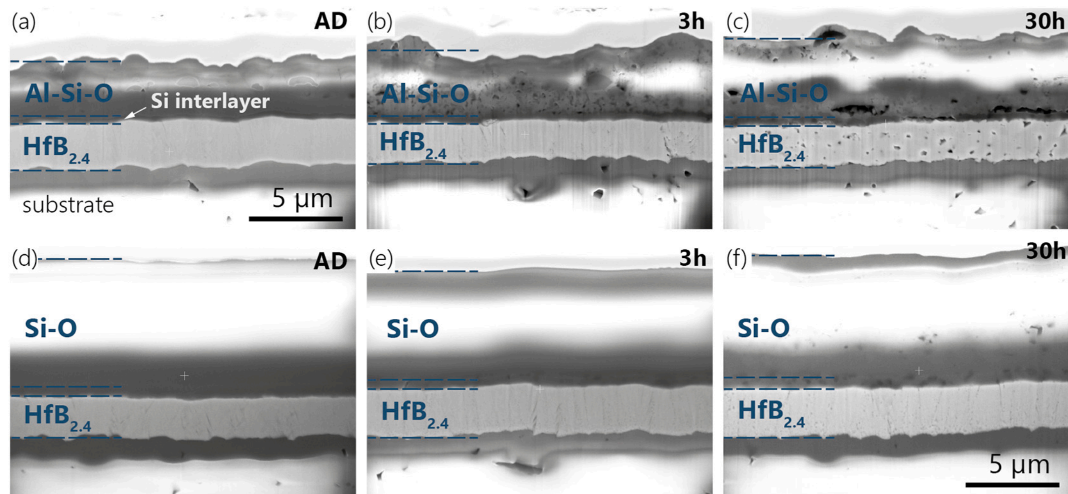

Fig. S2. FIB cross sections of $HfB_{2.4}$ thin films protected with (a–c) Si/Al-Si-O and (d–f) Si/Si-O top coatings. (a) and (d) show the as-deposited state for reference (AD), (b) and (e) after 3 h, (c) and (f) after 30 h of isothermal oxidation at 1200 °C in ambient air. All images were recorded on coated polycrystalline Al_2O_3 substrates.

References

[1] J.R. Rodgers, et al., Materials informatics, MRS Bull. 31 (2006) 975–980.
[2] B. Navinšek, et al., PVD coatings as an environmentally clean alternative to electroplating and electroless processes, Surf. Coat. Technol. 116–119 (1999) 476–487.
[3] S.-J. Lee, et al., Fabrication and properties of reactively hot pressed HfB_2-HfC ultra-high temperature ceramics, J. Korean Ceram. Soc. 47 (2010) 534–539, https://doi.org/10.4191/kcers.2010.47.6.534.
[4] W.G. Fahrenholtz, et al., Ultra-high temperature ceramics: materials for extreme environments, Scr. Mater. 129 (2017) 94–99.
[5] R. Savino, et al., Aero-thermo-chemical characterization of ultra-high-temperature ceramics for aerospace applications, J. Eur. Ceram. Soc. 38 (2018) 2937–2953.
[6] A. Nisar, et al., Ultra-high temperature ceramics: aspiration to overcome challenges in thermal protection systems, Ceram. Int. 48 (2022) 8852–8881.
[7] B.R. Golla, et al., Review on ultra-high temperature boride ceramics, Prog. Mater. Sci. 111 (2020), 100651.
[8] G.-J. Zhang, et al., Ultrahigh temperature ceramics (UHTCs) based on ZrB2 and HfB2 systems: powder synthesis, densification and mechanical properties, J. Phys. Conf. Ser. 176 (2009), 012041.
[9] W.G. Fahrenholtz, A historical perspective on research related to ultra-high temperature ceramics, in: Ultra-High Temperature Ceramics, John Wiley & Sons, Inc, Hoboken, NJ, 2014, pp. 6–32.
[10] M. Magnuson, et al., Review of transition-metal diboride thin films, Vacuum 196 (2022), 110567.
[11] X. Huang, et al., Investigation of mechanical properties and oxidation resistance of CVD TiB2 ceramic coating on molybdenum, J. Mater. Res. Technol. 9 (2020) 282–290.
[12] B. Bakhit, et al., Improving the high-temperature oxidation resistance of TiB2 thin films by alloying with Al, Acta Mater. 196 (2020) 677–689.
[13] T. Glechner, et al., Influence of the non-metal species on the oxidation kinetics of Hf, HfN, HfC, and HfB2 coatings, Mater. Des. 211 (2021), 110136.
[14] Y.-H. Koh, et al., Oxidation behavior of titanium boride at elevated temperatures, J. Am. Ceram. Soc. 84 (2001) 239–241.
[15] W.G. Fahrenholtz, et al., Oxidation of ultra-high temperature transition metal diboride ceramics, Int. Mater. Rev. 57 (2012) 61–72.
[16] T.A. Parthasarathy, et al., A model for the oxidation of ZrB2, HfB2 and TiB2, Acta Mater. 55 (2007) 5999–6010.
[17] R. Naraparaju, et al., Effect of moisture on the oxidation behavior of ZrB2, J. Am. Ceram. Soc. 104 (2021) 1058–1066.
[18] P. Sarin, et al., In situ studies of oxidation of ZrB2 and ZrB2–SiC composites at high temperatures, J. Eur. Ceram. Soc. 30 (2010) 2375–2386.
[19] T. Glechner, et al., Influence of Si on the oxidation behavior of TM-Si-B2±z coatings (TM = Ti, Cr, Hf, Ta, W), Surf. Coat. Technol. 434 (2022), 128178.
[20] L. Zauner, et al., Role of Si segregation in the structural, mechanical, and compositional evolution of high-temperature oxidation resistant Cr-Si-B2±z thin films, J. Alloys Compd. 944 (2023), 169203.
[21] T. Glechner, et al., Oxidation resistance of Si doped transition metal diborides at elevated temperatures, Int. J. Refract. Met. Hard Mater. 113 (2023), 106172.
[22] T. Glechner, et al., High temperature oxidation resistance of physical vapor deposited Hf-Si-B2±z thin films, Corros. Sci. 205 (2022), 110413.
[23] A. Bahr, et al., Oxidation behaviour and mechanical properties of sputter-deposited TMSi2 coatings (TM = Mo, Ta, Nb), J. Alloys Compd. 931 (2023), 167532.
[24] Z. Wu, et al., Improving oxidation and wear resistance of TiB2 films by nano-multilayering with Cr, Surf. Coat. Technol. 436 (2022), 128337.
[25] Plansee Composite Materials, Plansee Composite Materials. https://www.plansee.com/de/unternehmen/kontakt/deutschland.html (accessed January 10, 2023).
[26] C. Fuger, et al., Revisiting the origins of super-hardness in TiB2+z thin films – impact of growth conditions and anisotropy, Surf. Coat. Technol. 446 (2022), 128806.
[27] S. Dorri, et al., Oxidation kinetics of overstoichiometric TiB2 thin films grown by DC magnetron sputtering, Corros. Sci. 206 (2022), 110493.
[28] J. Neidhardt, et al., Experiment and simulation of the compositional evolution of Ti–B thin films deposited by sputtering of a compound target, J. Appl. Phys. 104 (2008), 063304.
[29] International Center of Diffraction Data, Powder Diffraction File - Cubic Al - 00-004-0787, 1954.
[30] B. Lönnberg, Thermal expansion studies on the group IV–VII transition metal diborides, J. Less Common Metals 141 (1988) 145–156.
[31] C.L. Jiang, et al., Determination of the thermal properties of AlB2-type WB2, Appl. Surf. Sci. 288 (2014) 324–330.
[32] CTE Al2O3 substrates, Kerafol. https://www.kerafol.com/_wpframe_custom/downloads/files/KERAFOL_Datenblatt_Keral99_07-17__095151-14012020.pdf (accessed September 4, 2023).
[33] H. Watanabe, et al., Linear thermal expansion coefficient of silicon from 293 to 1000 K, Int. J. Thermophys. 25 (2004) 221–236.
[34] H. Morkoç, Aluminum, gallium, and indium nitrides, in: Encyclopedia of Materials: Science And, 2001. https://ui.adsabs.harvard.edu/abs/2001emst.book..121M/abstract.
[35] J.S. Moya, et al., Sintering, in: R.A. Meyers (Ed.), Encyclopedia of Physical Science and Technology (Third Edition), Academic Press, New York, 2003, pp. 865–878.
[36] T.F. Choo, et al., A review on synthesis of mullite ceramics from industrial wastes, Recycl. Today 4 (2019) 39.
[37] L. Filipovic, Topography Simulation of Novel Processing Techniques, Technische Universität Wien, 2012. https://repositum.tuwien.at/handle/20.500.12708/13712. (Accessed 1 September 2023).
[38] International Center of Diffraction Data, Powder Diffraction File - Hexagonal WB2 - 04-003-6624, 2005.
[39] International Center of Diffraction Data, Powder Diffraction File - hexagonal TiB2 - 00-035-0741, 1985.
[40] International Center of Diffraction Data, Powder Diffraction File - Hexagonal HfB2 - 04-002-0174, 2005.
[41] International Center of Diffraction Data, Powder Diffraction File - Hexagonal Al2O3 - 01-088-5737, 2022.
[42] International Center of Diffraction Data, Powder Diffraction File - Cubic Si - 00-005-0565, 1955.
[43] International Center of Diffraction Data, Powder Diffraction File - Orthorhombic (Al2O3)3·2(SiO2) - 00-070-0189, 2020.
[44] International Center of Diffraction Data, Powder Diffraction File - Tetragonal TiO2 - 00-021-1276, 1970.
[45] International Center of Diffraction Data, Powder Diffraction File - Tetragonal SiO2 - 04-007-5015, 2005.
[46] International Center of Diffraction Data, Powder Diffraction File - hexagonal SiO2 - 01-085-0865, 1999.
[47] International Center of Diffraction Data, Powder Diffraction File - Monoclinic HfO2 - 00-034-0104, 1984.